THE CHEMICAL PROPERTIES OF LOW-REDSHIFT QSOS

JAEJIN SHIN[1], JONG-HAK WOO[1,5], TOHRU NAGAO[2,3], AND SANG CHUL KIM[4]
[1]Astronomy Program, Department of Physics and Astronomy, Seoul National University, Seoul, 151-742, Republic of Korea
[2]The Hakubi Center for Advanced Research, Kyoto University, Yoshida-Ushinomiya-cho, Sakyo-ku, Kyoto 606-8302, Japan
[3]Department of Astronomy, Kyoto University, Kitashirakawa-Oiwake-cho, Sakyo-ku, Kyoto 606-8502, Japan
[4]Korea Astronomy and Space Science Institute, Daejeon 305-348, Republic of Korea
Accepted for publication in ApJ

ABSTRACT

We investigate the chemical properties of low-z QSOs, using archival UV spectra obtained with the HST and IUE for a sample of 70 Palomar-Green QSOs at $z < 0.5$. By utilizing the flux ratio of UV emission lines (i.e., N V /C IV, (Si IV+O IV])/C IV, and N V/He II) as metallicity indicators, we compare broad-line region (BLR) gas metallicity with AGN properties, i.e., black hole mass, luminosity, and Eddington ratio. We find that BLR metallicity correlates with Eddington ratio while the dependency on black hole mass is much weaker. Although these trends of low-z AGNs appear to be different from those of high-z QSOs, the difference between low-z and high-z samples is partly caused by the limited dynamical range of the samples. We find that metal enrichment at the center of galaxies is closely connected to the accretion activity of black holes and that the scatter of metallicity correlations with black hole mass increases over cosmic time.

Subject headings: galaxies: active – galaxies: nuclei – galaxies: abundances – galaxies: evolution – quasars: emission lines

1. INTRODUCTION

Measuring chemical properties of galaxies and their redshift evolution is a crucial step in understanding galaxy evolution since the metallicity of galaxies is closely related to the history of star-formation, gas inflow, and outflow. A number of observational studies have been devoted to measure the metallicity of galaxies, revealing metallicity correlations with various galaxy properties. In the local universe, it has been shown that metallicity scales with galaxy luminosity and mass (the luminosity-metallicity relation and mass-metallicity relation, respectively) based on the metallicity measured from gas emission lines (Tremonti et al. 2004, and references therein) or stellar absorption lines (e.g., Gallazzi et al. 2005; Panter et al. 2008). These scaling relations indicate that metal enrichment is closely connected to the galaxy mass assembly.

Recently the redshift evolution of these scaling relations in star-forming galaxies has been extensively investigated. At $z < 3$, many studies have suggested apparent metallicity evolution as a function of redshift. The evolution is significant especially for low stellar-mass galaxies (e.q., Savaglio et al. 2005; Erb et al. 2006; Maiolino et al. 2008; Mannucci et al. 2009; Yabe et al. 2012), though it could be due to observational selection effects (see Mannucci et al. 2010). At $z > 3$, exploring the metallicity of galaxies is extremely challenging, because typical galaxies at such high redshifts are very faint and the classical metallicity indicators in the rest-frame optical spectra shift out of the atmospheric windows (but see also, e.g., Laskar et al. 2011; Nagao et al. 2012).

To extend the metallicity measurement toward higher redshifts, one possible approach is to focus on active galactic nuclei (AGNs). Thanks to their high luminosity (L_{AGN}) and a various metallic emission lines in their rest-frame ultraviolet spectra, it is possible to infer the metallicity of broadline regions (BLRs) even for QSOs at $z \sim 6-7$ with ground-based telescopes (Kurk et al. 2007; Juarez et al. 2009; see also Mortlock et al. 2011). Previously a positive relation between

[5] Author to whom any correspondence should be addressed

the metallicity of BLRs (Z_{BLR}) and the redshift of AGNs has been reported (e.g., Hamann & Ferland 1992, 1993); however it turned out that the apparent relation was caused by a selection bias and that the correlation between AGN luminosity and BLR metallicity (the $L_{AGN} - Z_{BLR}$ relation) was fundamental (see, e.g., Nagao et al. 2006b). Note that the luminosity-metallicity relation of AGNs has been also reported based on the emission lines in the narrow-line region (NLR), which is much more extended than BLR and traces the chemical properties in the spatial scale of AGN host galaxies (Nagao et al. 2006a; Matsuoka et al. 2009). Interestingly, the luminosity-metallicity relation of high-luminosity QSOs shows no strong redshift evolution in the redshift range of $2 < z < 6$ (Nagao et al. 2006a,b; Juarez et al. 2009; Matsuoka et al. 2011b), implying that the chemical evolution at the center of host galaxies is mostly completed at a very high redshift (see also Matsuoka et al. 2011a).

Although the observed $L_{AGN} - Z_{BLR}$ relation in AGNs and its redshift dependence are crucial to constrain evolutionary scenarios of the supermassive black hole (BH), the host galaxy, and the interplay between these two (i.e., the galaxy-BH coevolution), there are two main drawbacks that should be resolved. First, while the $L_{AGN} - Z_{BLR}$ relation is well established, its origin is still controversial. For example, Warner et al. (2004) reported that the metallicity of BLR showed a correlation with the mass of BH (M_{BH}), but no correlation with the Eddington ratio (L/L_{Edd}). Their result was recently confirmed by a larger sample of QSOs (Matsuoka et al. 2011b). On the other hand, Shemmer et al. (2004) claimed that the observed $L_{AGN} - Z_{BLR}$ relation was caused by the dependence of Z_{BLR} on the Eddington ratio, not on M_{BH} (see also Dietrich et al. 2009). At lower redshifts, it has been reported that narrow-line Seyfert 1 galaxies (NLS1s, whose Eddington ratios are believed to be high; see, e.g., Boroson 2002; Grupe 2004) show higher metallicity than typical broad-line AGNs (e.g., Wills et al. 1999; Nagao et al. 2002; Shemmer & Netzer 2002). The higher metallicity of NLS1s in these studies is qualitatively consistent with the re-

sult reported by Shemmer et al. (2004).

The other drawback comes from observational limitations. The AGN metallicity based on both BLRs and NLRs has been examined predominantly for AGNs at $z > 2$, since the AGN metallicity studies generally utilizes emission lines in the rest-frame ultraviolet spectra. Consequently, the observational studies with ground-based telescopes are limited to AGNs at $z > 2$. This prevents us from studying the difference in the chemical properties of BLRs between high-z and low-z QSOs. For instance, Nagao et al. (2006b) studied the $L_{\rm AGN} - Z_{\rm BLR}$ relation of QSOs at $2.0 \leq z \leq 4.5$. The possible physical origin of this $L_{\rm AGN} - Z_{\rm BLR}$ relation has been examined by Shemmer et al. (2004) for $2.0 < z < 3.5$, and by Matsuoka et al. (2011b) for $2.3 < z < 3.0$. Although Warner et al. (2004) investigate this issue for AGNs in a wide redshift range of $0 < z < 5$, they did not examine the redshift dependence of BLR chemical properties. Although there are a few attempts to infer the NLR metallicity based on the rest-frame optical spectra (e.q., Storchi-Bergmann et al. 1998; Nagao et al. 2002; Groves et al. 2006), those methods are in turn difficult to apply for high-z AGNs since infrared spectroscopy is required to obtain rest-frame optical emission lines, thus inconvenient for the comparative study between high and low redshifts. Using space observations with the *IUE* and the *HST*, Shemmer & Netzer (2002) investigated UV spectra of low-z AGNs and showed that a significant $L_{\rm AGN} - Z_{\rm BLR}$ relation was present also in low-z AGNs. However, they did not examine the physical origin of the $L_{\rm AGN} - Z_{\rm BLR}$ relation and thus it is not clear whether BH mass or the accretion rate derives the observed $L_{\rm AGN} - Z_{\rm BLR}$ relation, and whether the low-z and high-z AGNs show the same correlations.

Motivated by these considerations, in this paper we investigate the correlation between BLR metallicity with various AGN properties, including mass, luminosity, and Eddington ratio, for a sample of 70 low-z Palomar-Green (PG) QSO at $z < 0.5$, by utilizing the archival UV spectra. We describe the sample selection and the data in §2, the data analysis and the fitting procedure in §3. The main results are presented in §4, followed by discussion in §5 and summary and conclusions in §6. We adopt a cosmology of $H_0 = 70$ km s^{-1} Mpc^{-1}, $\Omega_\Lambda = 0.7$ and $\Omega_{\rm m} = 0.3$.

2. SAMPLE SELECTION AND THE DATA

2.1. *Sample selection*

To investigate metallicity of high-z QSOs, both permitted and weak semi-forbidden lines have been used. The weak semi-forbidden emission lines in the rest-frame UV spectra, i.e., N IV]λ1486, O III]λ1663, and N III]λ1749 are good metallicity indicators (e.g., Shields 1976; Baldwin & Netzer 1978; Osmer 1980; Uomoto 1984; Warner et al. 2002), since the flux ratio among these lines do not show strong dependences on physical properties of gas clouds (such as the density and ionization parameter). However, the actual application to observational data is generally difficult since those semi-forbidden emission lines are too faint to be measured accurately. Thus, stronger emission lines are preferred in the studies of $Z_{\rm BLR}$. For example, the flux ratios of N Vλ1240 to C IVλ1549 and N Vλ1240 to He IIλ1640 have been utilized to infer $Z_{\rm BLR}$ by comparing them with the prediction of photoionization models (e.q., Hamann & Ferland 1992, 1993; Ferland et al. 1996; Korista et al. 1998; Dietrich et al. 1999; Dietrich & Wilhelm-Erkens 2000; Hamann et al. 2002;

Dietrich et al. 2003). Nagao et al. (2006b) showed that the flux ratios of (Si IVλ1397+O IV]λ1402)/C IVλ1549 and Al IIIλ1857/C IVλ1549 are also useful to infer $Z_{\rm BLR}$ through photoionization model runs, that are used for inferring $Z_{\rm BLR}$ in high-z QSOs (e.g., Juarez et al. 2009; Matsuoka et al. 2011b).

Since most previous studies used the rest-frame UV spectra to infer BLR metallicity of high-redshift Type-1 QSOs, we therefore focus on high-luminosity QSOs at low-redshift, for which UV spectra are available, in order to investigate the chemical properties of low-z QSOs compared to high-z QSOs. The Palomar-Green (PG) QSOs (Schmidt & Green 1983) are well-studied low-z luminous Type-1 AGNs, and the UV spectra of many PG QSOs have been previously obtained with space facilities, thus suitable for our BLR metallicity study.

We selected all PG QSOs at $z < 0.5$ (89 objects), for which reliable black hole masses are available from either reverberation mapping results (Peterson et al. 2004; Denney et al. 2010) or single-epoch estimates (Vestergaard & Peterson 2006). To investigate BLR metallicity, we will use the flux ratios of N Vλ1240/C IVλ1549, N Vλ1240/He IIλ1640, and (Si IVλ1397+O IV]λ1402)/C IVλ1549, since these emission lines have relatively large equivalent widths. Thus, we searched for available UV spectra previously obtained from space facilities, using the Mikulski Archive for Space Telescopes (MAST). Among 89 PG QSOs at $z < 0.5$, the archival UV spectra covering the required emission lines were available for 86 objects. Among them, we excluded 7 broad absorption line (BAL) QSOs, since the strong absorption features prevent us from measuring the emission-line fluxes accurately. We also excluded 9 additional objects, for which the spectral quality is too low to identify the aforementioned emission lines. Thus, we finalized a sample of 70 PG QSOs for this work as listed in Table 1.

2.2. *Data*

We obtained the UV spectra taken with *International Ultraviolet Explorer* (*IUE*) or *Hubble Space Telescope* (*HST*) through the MAST database. We collected all available spectra of our targets and used the best quality spectrum with an order of *Cosmic Origins Spectrograph* (*COS*), *Space Telescope Imaging Spectrograph* (*STIS*), *Faint Object Spectrograph* (*FOS*), and *IUE* when multiple instruments have been used. In summary, we utilized 10 COS spectra, 4 STIS spectra, 26 for FOS and 30 *IUE* spectra.

Specifically, we used the SWP (1200−2000Å) data of *IUE*, G130H (1150−1600Å) and G160H (1600−2300Å) data of *HST*/FOS, and G140M (1150−1740Å) data of *HST*/STIS, for lower-z QSOs. For relatively higher-z QSOs, we used the LWP (1800−3200Å) data of *IUE* and G270H (2300−3200Å) data of *HST*/FOS data. Finally, for the *HST*/COS data, we used the combined data in two spectral ranges, i.e., G130M (1150−1450Å) and G160M (1405−1775Å), in order to cover the N V and C IV lines at the same time.

We combined the spectra of each exposures by calculating the error-weighted mean. For the STIS data, we combined the spectra using the exposure-time as a weight, because we could not eliminate artificial spark features effectively when we adopted the error-weighted mean. However, the spectra are qualitatively consistent. In the case of COS spectra, we used IDL routines developed by the COS GTO team (Danforth et al. 2010). We smoothed the spectra in the wavelength direction by adopting 7 pixel smoothing for the COS data and 2 pixel smoothing for the STIS data.

TABLE 1
LOG OF ARCHIVAL UV DATA & AGN PROPERTIES

Object (1)	Redshift (2)	Observation Date (3)	Telescope/Instrument (4)	$\log[M_{\mathrm{BH}}/M_\odot]$ (5)	Ref. (6)	$\log[L_{\mathrm{bol}}/\mathrm{erg\,s}^{-1}]$ (7)	S/N (8)
PG0003+158	0.450	1993 Nov 05,07	HST/FOS	9.25 ± 0.03	2	46.64 ± 0.18	5.47
PG0003+199	0.026	2010 Feb 08	HST/COS	7.13 ± 0.11	1	44.43 ± 0.04	28.09
PG0007+106	0.089	1981 Jun 08	IUE/SWP	8.71 ± 0.09	2	44.96 ± 0.10	7.30
PG0026+129	0.142	1994 Nov 27	HST/FOS	8.57 ± 0.11	1	45.57 ± 0.03	34.59
PG0049+171	0.064	1985 Jul 31	IUE/SWP	8.33 ± 0.09	2	44.36 ± 0.23	3.22
PG0050+124	0.061	1979 Dec 22,23	IUE/SWP	7.42 ± 0.10	2	44.69 ± 0.06	12.12
PG0052+251	0.155	1992 Jun 29	IUE/SWP	8.55 ± 0.09	1	45.78 ± 0.05	14.40
PG0157+001	0.164	1985 Aug 09	IUE/SWP	8.15 ± 0.09	2	45.70 ± 0.07	10.30
PG0804+761	0.100	2010 Jun 12	HST/COS	8.82 ± 0.05	1	45.99 ± 0.02	62.65
PG0838+770	0.131	2009 Sep 24	HST/COS	8.13 ± 0.09	2	45.24 ± 0.06	19.15
PG0844+349	0.064	1987 Nov 30;Dec 01	IUE/SWP	7.95 ± 0.18	1	45.00 ± 0.06	12.63
PG0921+525	0.035	1988 Feb 28,29	IUE/SWP	7.38 ± 0.11	1	44.30 ± 0.05	14.94
PG0923+129	0.029	1985 May 01	IUE/SWP	8.58 ± 0.10	2	44.14 ± 0.08	9.91
PG0947+396	0.206	1996 May 06	HST/FOS	8.66 ± 0.09	2	45.84 ± 0.14	6.78
PG1011–040	0.058	2010 Mar 26	HST/COS	7.30 ± 0.09	2	44.83 ± 0.03	35.03
PG1012+008	0.185	1990 Apr 10,	IUE/SWP	8.23 ± 0.09	2	45.41 ± 0.10	7.46
PG1022+519	0.045	1983 May 31;Jun 01	IUE/SWP	6.32 ± 0.19	1	44.48 ± 0.09	8.53
PG1048+342	0.167	1993 Nov 13	IUE/SWP	8.35 ± 0.09	2	44.74 ± 0.68	1.12
PG1049-005	0.357	1992 Apr 01,	HST/FOS	9.16 ± 0.09	2	46.17 ± 0.22	4.36
PG1103–006	0.425	1992 Dec 29	HST/FOS	9.30 ± 0.10	2	46.11 ± 0.11	8.68
PG1115+407	0.154	1996 May 19	HST/FOS	7.65 ± 0.09	2	45.62 ± 0.08	12.30
PG1116+215	0.177	1993 Feb 19,20	HST/FOS	8.51 ± 0.09	2	46.30 ± 0.15	6.56
PG1119+120	0.049	1982 Nov 21,26	IUE/SWP	7.45 ± 0.09	2	44.62 ± 0.06	12.89
PG1121+422	0.234	1995 Jan 08	IUE/SWP	8.01 ± 0.09	2	45.94 ± 0.11	7.06
PG1149–110	0.049	1992 Dec 29	IUE/SWP	7.90 ± 0.10	2	44.25 ± 0.10	7.58
PG1151+117	0.176	1987 Jan 29,30	IUE/SWP	8.53 ± 0.09	2	45.65 ± 0.11	6.68
PG1202+281	0.165	1996 Jul 21	HST/FOS	8.59 ± 0.09	2	44.95 ± 0.14	7.07
PG1211+143	0.085	2002 Feb 04,07	HST/STIS	7.94 ± 0.09	2	45.63 ± 0.04	19.41
PG1216+069	0.334	1993 Mar 15	HST/FOS	9.18 ± 0.09	2	46.52 ± 0.14	7.03
PG1226+023	0.158	1991 Jul 9	HST/FOS	8.93 ± 0.09	1	46.59 ± 0.09	10.60
PG1229+204	0.063	1982 May 01,02	IUE/SWP	7.84 ± 0.21	1	45.11 ± 0.04	21.02
PG1244+026	0.048	1983 Feb 08	IUE/SWP	6.50 ± 0.09	2	44.30 ± 0.10	7.72
PG1259+593	0.472	1991 Dec 27	HST/FOS	8.90 ± 0.10	2	46.76 ± 0.23	4.15
PG1302-102	0.286	1986 Jul 25,26	IUE/SWP, LWP	8.86 ± 0.10	2	46.45 ± 0.01	57.25
PG1307+085	0.155	1980 May 04	IUE/SWP	8.62 ± 0.12	1	45.80 ± 0.07	10.33
PG1310–108	0.035	1995 Feb 11	IUE/SWP	7.86 ± 0.09	2	44.13 ± 0.10	7.66
PG1322+659	0.168	1997 Jan 19	HST/FOS	8.26 ± 0.11	2	45.52 ± 0.04	23.02
PG1341+258	0.087	1995 Mar 22	IUE/SWP	8.02 ± 0.10	2	44.71 ± 0.13	5.70
PG1351+695	0.030	2011 Jun 27	HST/COS	7.52 ± 0.12	1	43.63 ± 0.10	8.61
PG1352+183	0.158	1996 May26	HST/FOS	8.40 ± 0.09	2	45.60 ± 0.11	8.52
PG1402+261	0.164	1996 Aug 25	HST/FOS	7.92 ± 0.09	2	45.95 ± 0.08	12.85
PG1404+226	0.098	1996 Feb 23	HST/FOS	6.87 ± 0.09	2	44.86 ± 0.15	6.62
PG1415+451	0.114	1997 Jan 02	HST/FOS	7.99 ± 0.09	2	45.29 ± 0.08	12.11
PG1416–129	0.129	1988 Mar 03	IUE/SWP	9.02 ± 0.09	2	44.93 ± 0.17	4.51
PG1425+267	0.366	1996 Jun29	HST/FOS	9.71 ± 0.11	2	46.15 ± 0.06	17.63
PG1426+015	0.086	2004 Jul 27, 28, 29	HST/STIS	9.09 ± 0.13	1	45.63 ± 0.07	10.18
PG1427+480	0.221	1997 Jan 07	HST/FOS	8.07 ± 0.09	2	45.75 ± 0.10	9.61
PG1434+590	0.031	2009 Aug 04	HST/COS	7.77 ± 0.12	1*	44.93 ± 0.03	37.65
PG1435–067	0.129	1995 Jun 12	IUE/SWP	8.34 ± 0.09	2	45.56 ± 0.09	8.74
PG1440+356	0.077	1996 Dec 05	HST/FOS	7.45 ± 0.09	2	45.59 ± 0.06	17.75
PG1444+407	0.267	1996 May 23	HST/FOS	8.27 ± 0.09	2	46.24 ± 0.10	9.54
PG1448+273	0.065	2011 Jun 18	HST/COS	6.95 ± 0.09	2	44.36 ± 0.03	13.07
PG1501+106	0.036	1989 Jun 30; Jul 02	IUE/SWP	8.50 ± 0.09	2	44.51 ± 0.03	29.62
PG1512+370	0.371	1992 Jan 26	HST/FOS	9.35 ± 0.09	2	46.36 ± 0.17	5.66
PG1519+226	0.137	1995 Jun 11	IUE/SWP	7.92 ± 0.09	2	45.16 ± 0.18	4.27
PG1534+580	0.030	2009 Oct 28	HST/COS	7.37 ± 0.07	1*	44.16 ± 0.05	22.45
PG1543+489	0.400	1995 Mar 14	HST/FOS	7.98 ± 0.09	2	46.26 ± 0.04	28.04
PG1545+210	0.266	1992 Apr 08,10	HST/FOS	9.29 ± 0.09	2	45.98 ± 0.10	10.04
PG1552+085	0.119	1986 Apr 28	IUE/SWP	7.52 ± 0.09	2	44.81 ± 0.24	3.14
PG1612+261	0.131	1980 Sep 10	IUE/SWP	8.04 ± 0.09	2	45.07 ± 0.15	5.13
PG1613+658	0.129	2010 Apr 08, 09, 10	HST/COS	8.43 ± 0.20	1	45.94 ± 0.02	53.54
PG1617+175	0.112	1993 May 13	IUE/SWP	8.75 ± 0.10	1	45.24 ± 0.09	8.66
PG1626+554	0.133	1997 Nov 19	HST/FOS	8.48 ± 0.09	2	45.72 ± 0.07	14.30
PG2112+059	0.466	1992 Sep 19	HST/FOS	8.98 ± 0.10	2	46.25 ± 0.18	5.53
PG2130+099	0.063	2010 Oct 28,	HST/COS	8.64 ± 0.05	1	44.92 ± 0.03	34.83
PG2214+139	0.067	1984 Jun 03	IUE/SWP	8.53 ± 0.10	2	44.39 ± 0.84	0.89
PG2233+134	0.325	2003 May 13	HST/STIS	8.02 ± 0.09	2	46.16 ± 0.04	21.26
PG2251+113	0.323	2001 May 01	HST/STIS	8.97 ± 0.09	2	45.83 ± 0.05	14.15
PG2304+042	0.042	1989 Dec 29	IUE/SWP	8.54 ± 0.10	2	43.72 ± 0.25	3.03
PG2308+098	0.432	1992 Oct 12	HST/FOS	9.57 ± 0.11	2	46.33 ± 0.18	5.38

NOTE. — Col. (1): Target ID. Col. (2): Redshift. Col. (3): Observed date. Col. (4): Telescope and Instrument. Col. (5): Black hole mass from Peterson et al. (2004); Vestergaard & Peterson (2006); Denney et al. (2010) with a new virial factor (Woo et al. 2010). Col. (6): References for redshift and black hole mass. 1 - Reverberation-mapped AGNs (Peterson et al. 2004), 1* - Reverberation-mapped AGNs (Denney et al. 2010), 2 - AGNs with single-epoch black hole mass (Vestergaard & Peterson 2006). Col. (7): AGN bolometric luminosity calculated from the monochromatic luminosity at 1350Å by multiplying a bolometric correction factor, 3.81. Col. (8): Signal-to-noise ratio per resolution element at 1350Å in the rest-frame.

If a target has been observed at multiple-epochs, we chose only one epoch with the best data quality to avoid any time-variation effects. Table 1 lists the observation data and the instrument for each target. In this table we also list the signal-to-noise ratio per resolution element calculated at the rest-frame 1350Å continuum.

2.3. *AGN properties*

To compare with BLR metallicity, we measure and collect other AGN properties, i.e., black hole mass, bolometric luminosity, and Eddington ratio. We collected black hole mass of the sample QSOs, which has been previously determined by the reverberation mapping studies for 18 objects (Peterson et al. 2004; Denney et al. 2010) or by the single-epoch method for 52 objects (Vestergaard & Peterson 2006). A black hole mass measurement based on reverberation-mapping results is availble for PG1211+143 (Peterson et al. 2004), however it has large uncertainty due to the low data quality, and it has been excluded in other reverberation sample studies. Thus, we will use single-epoch mass for PG1211+143.

We re-calculated black hole mass of the sample by adopting the updated virial factor of 5.2 (Woo et al. 2010), which is slightly smaller than the previous virial factor (5.5; Onken et al. 2004, see also Park et al. 2012)

As the uncertainty of black holes masses, we adopted the values given by Peterson et al. (2004); Vestergaard & Peterson (2006); Denney et al. (2010).

For AGN bolometric luminosity (L_{AGN}), we used the obtained UV spectra to measure monochromatic luminosity at 1350Å, which is presumably not heavily contaminated by the host galaxy stellar light. To measure the flux at 1350Å, we fitted the AGN continuum between 1210Å and 1700Å with a power-law function. The measured 1350Å monochromatic continuum luminosity is then used for calculating AGN bolometric luminosity by multiplying a bolometric correction factor, 3.81 (Shen et al. 2008). Note that this bolometric correction factor is the same as adopted by Matsuoka et al. (2011b) for high-z QSOs. The measurement uncertainty of AGN luminosities was calculated based on the signal-to-noise ratio of the spectra.

In Figure 1, we present the distribution of the sample properties; the redshift, black hole mass, bolometric luminosity, and Eddington ratio. The black hole mass ranges over 3 orders of magnitude (from 6.32 to 9.71) with an average of $8.26 \pm 0.71\,M_\odot$. The bolometric luminosity also ranges over a large range from $10^{43.6}$ to $10^{46.8}$ erg s^{-1} while some fraction of the sample has relatively low luminosity and belong to Seyfert class rather than QSOs. The mean Eddington ratio of the sample is ∼10% with 0.66 dex dispersion, indicating that there is a large range of accretion activity (Woo & Urry 2002).

3. ANALYSIS

3.1. *Multi-component fitting procedure*

The flux measurement of BLR emission lines is an important step for investigating Z_{BLR}. It is known that BLR emission lines sometimes show significant asymmetric velocity profiles (e.g., Corbin 1997; Vanden Berk et al. 2001; Baskin & Laor 2005), hence a single-Gaussian model does not generate a reliable fit for such cases. To fit asymmetric velocity profiles of QSO UV emission lines, various models have been adopted. Here, we examined 4 mod-
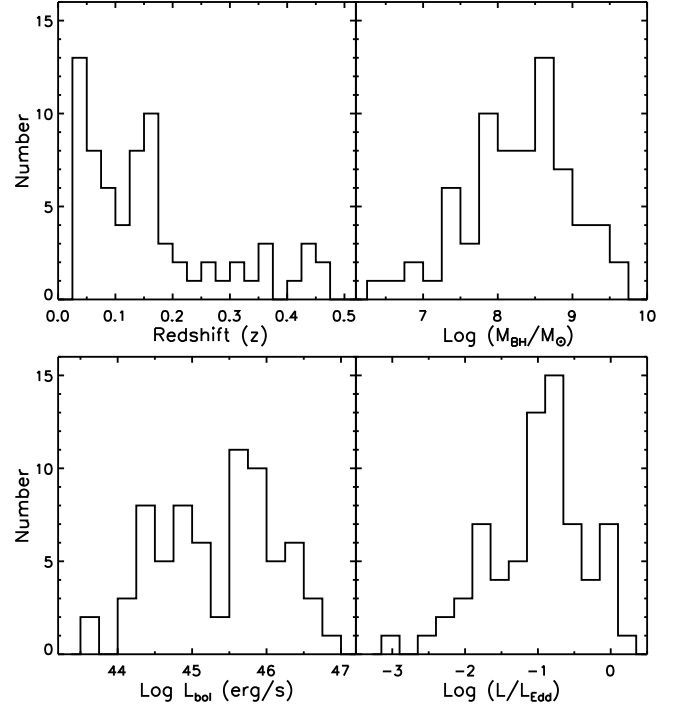

FIG. 1.— The distributions of the redshift, BH mass, AGN luminosity, and the Eddington ratio of the sample.

els, namely, double-Gaussian, Gauss-Hermitian, modified-Lorentzian, and 2 power-law functions to determine the best line profile to use. In Figure 2, we present the C IV line of PG0003+158 as well as 4 different model fits, which show slightly different results, particularly at the wing of the line. Through our visual inspection, we decided to adopt the double-Gaussian function as an emission line profile model. Note that our results do not significantly depend on the choice of the model since the difference in flux measurements is ∼ 5%.

In the rest-frame UV spectra, many AGN emission lines are blended; Lyα λ1216+N Vλ1240, Si IVλ1397+O IV]λ1402, and He IIλ1640+O III]λ1663+Al IIλ1671. Thus, it is necessary to perform a multi-component fitting analysis for secure flux measurements. We simultaneously fitted all 10 emission lines, that were used as BLR metallicity indicators. First, we divided these emission lines into two groups based on their ionization degree, and assumed that the emission lines in each group have the same velocity profile (see Nagao et al. 2006b). Specifically, we categorized N Vλ1240, O IV]λ1402, N IV]λ1486, C IVλ1549 and He IIλ1640) in the high-ionization group, while Si IIλ1263, Si IVλ1397, O III]λ1663 and Al IIλ1671 in the low-ionization group, following Nagao et al. (2006b). We adopted the same velocity width and the velocity shift for each group. We excluded the spectral range between 1570Å and 1631Å from the fit, since an unidentified emission feature is reported in this range (see, e.g., Wilkes 1984; Boyle 1990; Laor et al. 1994; Nagao et al. 2006b). In the case of Lyα, the absorption by the intergalactic matter (IGM) affects the line profile significantly, particularly below 1210Å. Thus, we treated Lyα separately, by allowing the velocity dispersion and velocity shift to be free. We excluded the spectral range below 1210Å from the fitting procedure, because of the IGM absorption. For the continuum fitting, we used a power-law and determined the slope
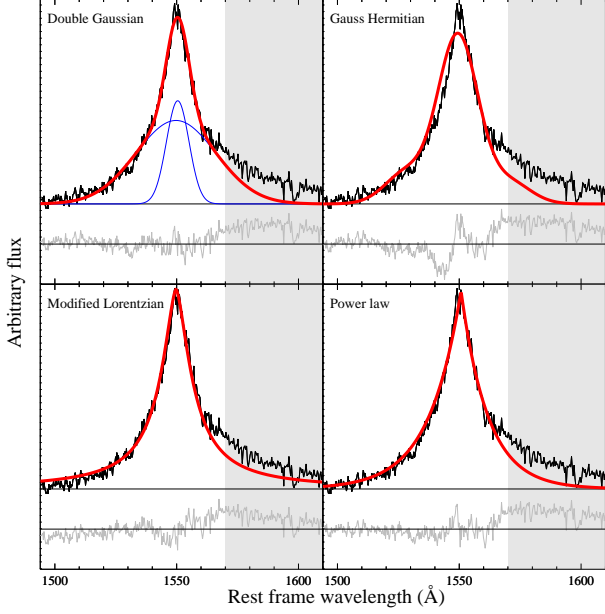
FIG. 2.— Comparison of different fitting functions for the C IVλ1549 emission line of PG 0003+158. Double-Gaussian (upper left), Gauss-Hermitian (upper right), modified-Lorentzian (lower left) and 2 power-law (lower right) functions are examined. The red lines denote the fitting results, and the blue line in the upper left panel represents each Gaussian component. Residual spectrum is shown at the bottom in each panel. Masked regions are indicated with gray hatches.
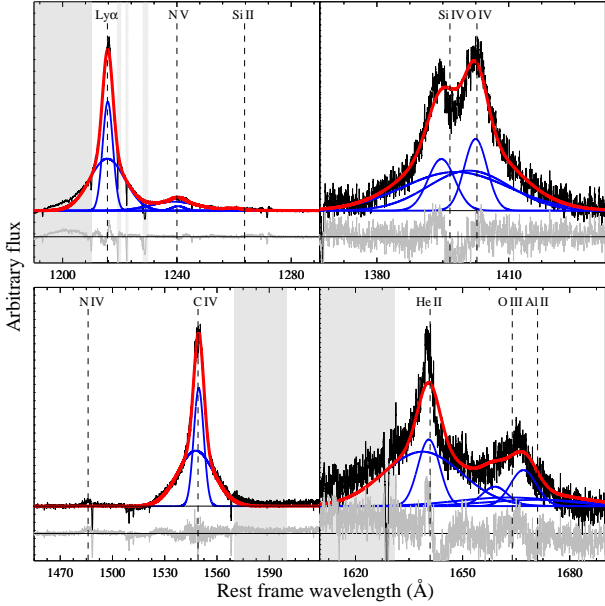

FIG. 3.— Examples of Multi-component fitting analysis. Each panel shows Lyα λ1216+N Vλ1240 (upper left), Si IVλ1397+O IV]λ1402 (upper right), N IV]λ1486+C IVλ1549 (bottom left), and He IIλ1640+O III]λ1663+Al IIλ1671 (bottom right), respectively. The color of lines are the same as in Figure 2. The dashed lines indicate the center of each emission line.

by using three spectral windows (1345Å – 1355Å, 1445Å – 1455Å, and 1687Å – 1697Å), where no strong emission lines are present.

Figure 3 shows examples of multi-component fitting for 4 different spectral regions: from upper left to bottom right, 1) Lyα λ1216+N Vλ1240, 2) Si IVλ1397+O IV]λ1402, 3) N IV]λ1486+C IVλ1549,
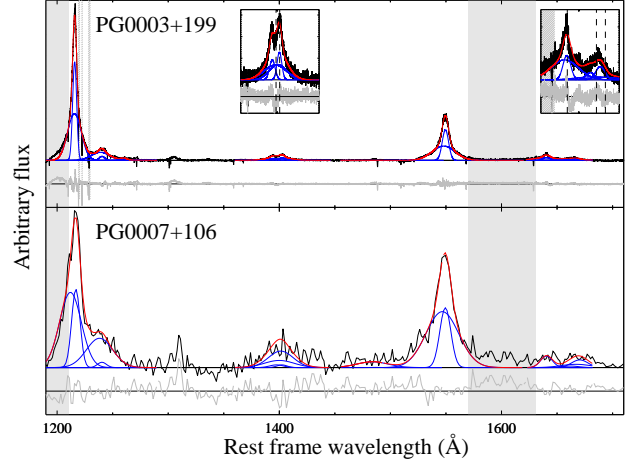

FIG. 4.— Fitting results of 2 representative objects: PG 0003+018 with a high quality COS spectrum (top) and PG 0007+106 with a low quality IUE spectrum (bottom). The inset panels show the fit for weak lines, namely, Si IV+O IV] (left) and He II+O III]+Al II (right). No inset panel means that fluxes of these weak lines were not measured due to the low signal-to-noise ratio. The green dashed lines in the inset panels represent the center of each line as shown in Figure 3. The fitting residual is shown in the lower panel for each object. The color of lines and masked regions are the same as in Figure 2.

and 4) He IIλ1640+O III]λ1663+Al IIλ1671. The line center is denoted with dashed lines.

3.2. *Fitting result*

Based on the multi-component fitting using double-Gaussian profiles, we measured the flux of 10 broad emission lines in the rest-frame UV spectra for the sample. In Figure 4, we present the fitting results of 2 representative targets; PG 0003+199 with high quality COS data and PG 0007+106 with low quality IUE data. In some cases, spectral quality is too low to fit the weak emission lines, i.e., N Vλ1240, Si IVλ1397, O IV]λ1402, C IVλ1549, and He IIλ1640, thus we only measure the flux of N V and C IV. The weak lines (i.e., Si IV+O IV] and He II+O III]+Al II) are shown in the inset panels only when these lines were successfully fitted. In summary, we measured the N V and C IV fluxes for the entire sample (70 objects) while we measured the flux of Si IV, O IV], He II for a subsample of 34 objects. Table 2 lists the measured fluxes and the inferred uncertainties, which were estimated by averaging the signal-to-noise ratio of each pixel within the spectral range of each lines. We list the sum of Si IVλ1397 and O IV]λ1402 fluxes instead of individual flux measurements, since the sum of two lines will be used to compare with the flux of the C IV line.

4. RESULT

4.1. *Comparison of emission-line fluxes*

In this study, we use three line flux ratios as metallicity indicators among various diagnostics previously proposed, due to the limited data quality; namely, N Vλ1240/C IVλ1549, (Si IVλ1397+O IV]λ1402)/C IVλ1549, and N Vλ1240/He IIλ1640 (hereafter N V/C IV, (Si IV+O IV])/C IV, and N V/He II, respectively). Before using them as metallicity indicators in comparison with AGN properties, here we first examine the correlation among the emission line fluxes.

Figure 5 (top panel) presents the comparison between the C IVλ1549 and He IIλ1640 fluxes, which are used as a

TABLE 2
MEASUREMENTS OF EMISSION LINE FLUXES

Object	N V	Si IV+O IV] (10^{-14} erg s^{-1})	C IV	He II
(1)	(2)	(3)	(4)	(5)
PG0003+158	32.9 ± 5.6	10.6 ± 1.2	70.0 ± 8.7	8.9 ± 1.2
PG0003+199	90.4 ± 2.9	52.7 ± 1.1	280.8 ± 12.1	39.6 ± 1.9
PG0007+106	34.2 ± 2.6	—	104.5 ± 6.0	—
PG0026+129	48.0 ± 1.1	—	57.2 ± 2.9	6.3 ± 0.3
PG0049+171	16.1 ± 3.9	—	126.5 ± 30.8	—
PG0050+124	56.0 ± 3.0	26.0 ± 1.5	47.0 ± 2.6	—
PG0052+251	59.4 ± 3.0	—	120.2 ± 3.9	5.2 ± 0.2
PG0157+001	29.2 ± 2.1	—	64.0 ± 2.8	3.8 ± 0.2
PG0804+761	214.1 ± 3.0	98.2 ± 1.2	240.0 ± 5.8	—
PG0838+770	14.6 ± 0.4	10.2 ± 0.6	32.7 ± 2.4	—
PG0844+349	69.0 ± 3.9	—	112.5 ± 6.6	—
PG0921+525	39.7 ± 1.9	46.9 ± 2.8	292.0 ± 12.9	13.7 ± 0.5
PG0923+129	66.3 ± 5.0	—	183.3 ± 15.8	18.4 ± 1.3
PG0947+396	32.9 ± 2.0	11.5 ± 0.7	59.5 ± 2.6	7.3 ± 0.3
PG1011−040	27.8 ± 0.8	14.6 ± 0.4	38.8 ± 2.4	5.6 ± 0.4
PG1012+008	8.6 ± 0.9	17.7 ± 1.5	22.2 ± 1.6	—
PG1022+519	12.2 ± 1.1	—	45.7 ± 4.5	—
PG1048+342	12.4 ± 2.9	—	19.1 ± 3.4	—
PG1049−005	29.7 ± 7.3	11.3 ± 1.9	41.6 ± 6.4	4.7 ± 0.7
PG1103−006	13.8 ± 1.6	—	13.8 ± 0.9	0.7 ± 0.1
PG1115+407	18.5 ± 1.2	—	34.4 ± 2.0	—
PG1116+215	148.5 ± 20.5	78.3 ± 14.4	210.9 ± 28.1	17.1 ± 2.2
PG1119+120	52.2 ± 2.6	18.4 ± 1.3	73.2 ± 4.3	8.0 ± 0.4
PG1121+422	14.5 ± 1.9	—	47.8 ± 3.5	—
PG1149−110	17.1 ± 1.4	—	92.6 ± 7.4	—
PG1151+117	35.9 ± 3.9	—	51.1 ± 3.5	6.6 ± 0.5
PG1202+281	8.3 ± 0.8	—	72.9 ± 5.1	—
PG1211+143	80.6 ± 3.3	27.5 ± 1.0	171.0 ± 12.1	—
PG1216+069	50.8 ± 8.7	19.3 ± 2.1	105.6 ± 9.6	10.6 ± 0.9
PG1226+023	168.0 ± 17.1	59.8 ± 3.0	305.5 ± 13.5	32.3 ± 1.4
PG1229+204	15.0 ± 0.6	47.5 ± 2.0	156.4 ± 4.8	11.4 ± 0.3
PG1244+026	3.7 ± 0.3	—	11.4 ± 1.2	—
PG1259+593	25.5 ± 6.0	13.9 ± 2.0	28.1 ± 4.3	2.4 ± 0.3
PG1302−102	46.8 ± 1.0	—	52.4 ± 0.6	—
PG1307+085	64.3 ± 4.2	—	114.6 ± 4.6	—
PG1310−108	36.4 ± 3.4	—	140.3 ± 15.2	26.1 ± 2.4
PG1322+659	31.1 ± 1.2	—	51.4 ± 2.1	6.6 ± 0.3
PG1341+258	22.4 ± 2.6	—	34.7 ± 5.3	—
PG1351+695	18.1 ± 1.8	10.9 ± 0.7	99.6 ± 11.1	5.3 ± 0.9
PG1352+183	29.9 ± 2.6	—	47.4 ± 2.8	—
PG1402+261	15.0 ± 1.0	—	68.9 ± 3.4	—
PG1404+226	9.5 ± 1.3	—	13.1 ± 1.6	—
PG1415+451	44.0 ± 2.7	20.4 ± 1.1	55.0 ± 2.8	6.6 ± 0.3
PG1416−129	6.7 ± 0.9	—	66.4 ± 4.3	—
PG1425+267	8.6 ± 0.4	—	49.4 ± 1.5	—
PG1426+015	94.3 ± 6.8	—	260.7 ± 36.8	—
PG1427+480	13.8 ± 0.7	9.3 ± 0.4	43.1 ± 2.0	6.1 ± 0.3
PG1434+590	186.9 ± 4.2	86.7 ± 1.4	379.3 ± 16.2	—
PG1435−067	32.3 ± 2.6	—	62.4 ± 4.1	—
PG1440+356	96.1 ± 5.1	54.7 ± 2.2	119.1 ± 4.9	20.9 ± 0.7
PG1444+407	36.0 ± 2.1	—	32.6 ± 2.8	—
PG1448+273	10.0 ± 0.8	3.7 ± 0.2	13.2 ± 1.5	4.1 ± 0.5
PG1501+106	18.0 ± 0.5	—	219.0 ± 5.6	9.8 ± 0.2
PG1512+370	32.9 ± 5.8	8.3 ± 1.0	70.2 ± 7.3	4.5 ± 0.8
PG1519+226	22.4 ± 3.4	29.0 ± 6.0	49.0 ± 5.9	—
PG1534+580	40.8 ± 1.5	25.1 ± 0.5	187.5 ± 6.0	14.3 ± 0.6
PG1543+489	25.7 ± 0.9	11.8 ± 0.3	23.7 ± 0.5	—
PG1545+210	36.9 ± 2.0	—	101.6 ± 5.4	6.9 ± 0.4
PG1552+085	12.7 ± 2.2	—	30.7 ± 4.4	—
PG1612+261	11.0 ± 1.3	—	67.8 ± 5.1	2.5 ± 0.1
PG1613+658	63.7 ± 1.2	19.2 ± 0.4	175.7 ± 4.5	—
PG1617+175	12.5 ± 1.2	—	41.2 ± 2.1	—
PG1626+554	55.0 ± 3.0	18.5 ± 1.0	78.9 ± 3.8	5.7 ± 0.3
PG2112+059	23.8 ± 3.8	9.1 ± 1.1	16.0 ± 2.0	—
PG2130+099	34.9 ± 0.9	—	120.8 ± 6.7	14.9 ± 0.9
PG2214+139	9.8 ± 2.7	—	88.8 ± 14.3	8.0 ± 1.5
PG2233+134	10.4 ± 0.8	4.4 ± 0.2	8.0 ± 0.3	—
PG2251+113	21.0 ± 2.2	5.3 ± 0.2	29.4 ± 1.2	—
PG2304+042	12.5 ± 1.6	—	89.2 ± 8.8	—
PG2308+098	23.5 ± 4.5	6.4 ± 0.8	37.0 ± 4.8	—

NOTE. — Col. (1): Target ID. Col. (2): line flux and error of N V. Col. (3): line flux and error of Si IV+O IV. Col. (4): line flux and error of C IV. Col. (5): line flux and error of He II.

denominator of metallicity diagnostics. As photoionization models predict that the flux ratio of these two lines does not depend on $Z_{\rm BLR}$ (see, e.g., Figure 29 in Nagao et al. 2006b), a clear linear relation with a small scatter (0.20 dex) is present, showing that the flux ratio of these two lines is nearly constant. The constant flux ratio between C IV and He II suggests that our flux measurements of the weak He II line are reasonable although the He II is difficult to fit due to blending with Al II.

In Figure 5 (bottom panel) we compare the N Vλ1240 flux and the sum of the Si IVλ1397 and O IV]λ1402 fluxes, which are used as a numerator of metallicity indicators. Again a clear positive correlation is present between them, with a somewhat larger scatter than that shown in the comparison between the C IV and He II fluxes. This larger scatter is partly caused by the fact that the N V flux depends on $Z_{\rm BLR}$ as well as the relative abundance of N V (see, e.g., Matsuoka et al. 2011b; Araki et al. 2012), while the sum of the Si IV and O IV] fluxes mainly depends on $Z_{\rm BLR}$.

4.2. Comparison among metallicity indicators

We compare 3 line flux ratios, namely, N V/C IV, (Si IV+O IV])/C IV, and N V/He II, as metallicity indicators adopted in this study. As shown in Figure 6, the flux ratios of N V/C IV and N V/He II present a clear correlation with a relatively small scatter, reflecting the constant flux ratio between C IV and He II (see Figure 5). The comparison between (Si IV+O IV])/C IV and N V/C IV also shows a relatively good correlation although a few outliers dominate the scatter. In the case of (Si IV+O IV])/C IV and N V/He II, the comparison shows a less clear correlation, probably due to the larger combined uncertainties on the flux measurements of weak lines (Si IV+O IV] and He II).

4.3. Comparison between metallicity and AGN properties

In this section, we investigate the correlation between BLR metallicity inferred from the emission line ratios and AGN properties, i.e., black hole mass, luminosity, and Eddington ratio, using the selected low-z QSOs. Figure 7 compares 3 metallicity indicators (N V/C IV, (Si IV+O IV])/C IV, and N V/He II) with AGN properties ($M_{\rm BH}$, $L_{\rm bol}$, and $L_{\rm bol}/L_{\rm Edd}$), respectively. A positive correlation is present between N V/C IV or N V/He II with AGN luminosity, indicating a luminosity dependence of the BLR metallicity, while it is less certain in the case of (Si IV+O IV])/C IV, probably due to the larger measurement uncertainty in Si IV+O IV] flux. The apparent luminosity - BLR metallicity correlation of low redshift QSOs is similar to the results from previous studies based on high redshift AGNs (Shemmer et al. 2004; Warner et al. 2004; Nagao et al. 2006b).

We investigate which parameter between $M_{\rm BH}$ and $L_{\rm bol}/L_{\rm Edd}$ is more fundamental in driving the observed $L_{\rm AGN} - Z_{\rm BLR}$ relation. As for $M_{\rm BH}$, there is no obvious $M_{\rm BH}$ dependence on N V/C IV and (Si IV+O IV])/C IV while there is a possible positive correlation between N V/He II and $M_{\rm BH}$. These behaviors are in contrast to previous results obtained at high redshifts, where significant positive correlations were reported between the metallicity indicators and $M_{\rm BH}$ (Warner et al. 2004; Matsuoka et al. 2011b).

On the contrary, clear positive dependences on $L_{\rm bol}/L_{\rm Edd}$ are present in N V/C IV and N V/He II, while it is less certain in the case of (Si IV+O IV])/C IV, due to the lack of objects in the range of $L_{\rm bol}/L_{\rm Edd} < -1.5$. For these low Eddington
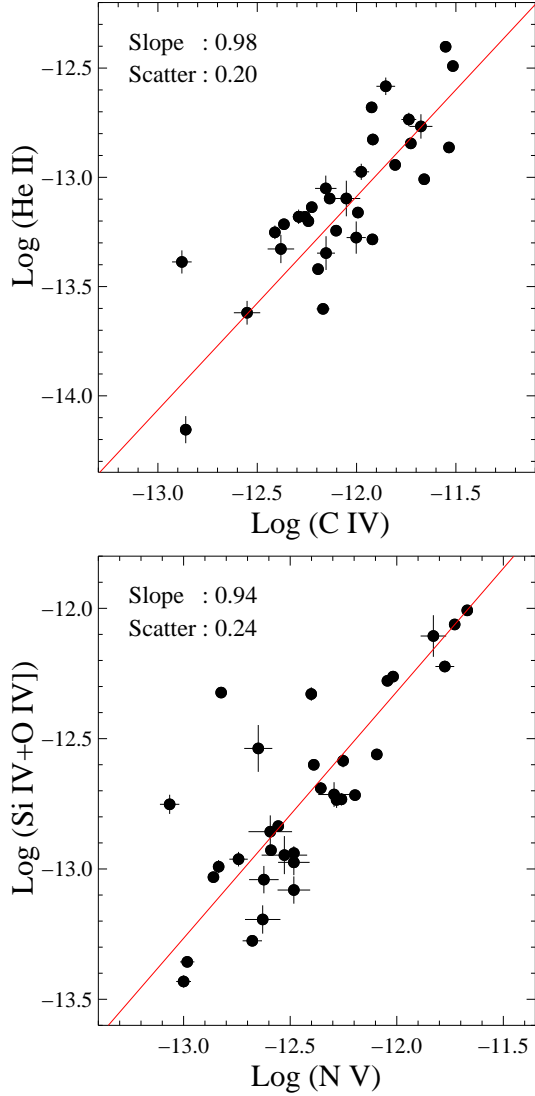
FIG. 5.— Comparison of emission-line fluxes. *Top:* Comparison between the He IIλ1640 and C IVλ1549 fluxes. *Bottom:* Comparison between the sum of the Si IVλ1397 and O IV]λ1402 fluxes and N Vλ1240 flux. The derived Spearman's rank order correlation coefficients and their statistical significance are +0.795, 3.2×10^{-8} (top) and +0.751, 4.5×10^{-7} (bottom).

ratio objects, Si IV+O IV] lines are very weak and no secure measurements are available.

In order to examine the statistical significance of these possible correlations, we applied the Spearman's rank-order test to the data. The derived Spearman's rank-order correlation coefficients (r_S) and their statistical significance (p), which is the probability of the data being consistent with the null hypothesis that the flux ratio is not correlated with an AGN parameter, are given in Table 3. The rank-order tests suggest that there are statistically significant positive correlations of N V/C IV with L_{bol} and L_{bol}/L_{Edd}, and a positive correlation of N V/He II with L_{bol}. In contrast, all three diagnostic flux ratios show no statistically significant correlation with M_{BH}.

5. DISCUSSION

We compare our results obtained for AGNs at $z < 0.5$ with the previous results obtained for high-z QSOs ($z \sim 2.5$; Matsuoka et al. 2011b), in order to investigate possible red-
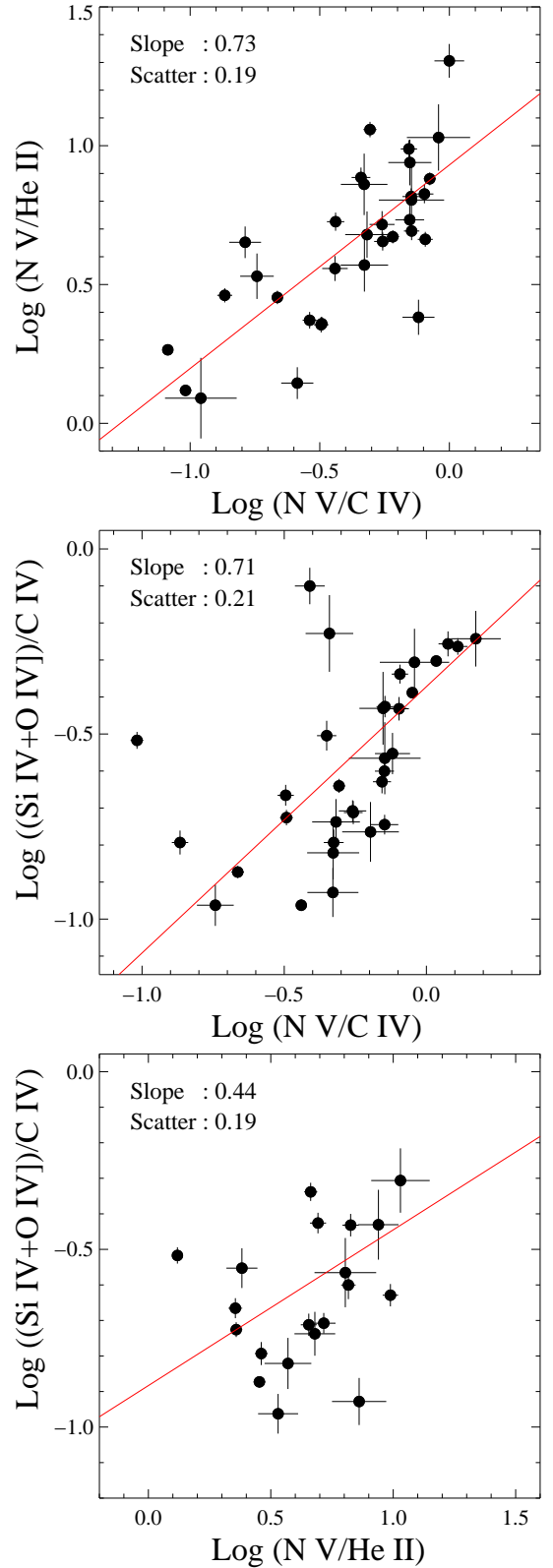

FIG. 6.— The relation among three metallicity indicators. Red line represents error weighted linear fit to the data. The slopes of the linear fit and the data dispersion are shown at the upper-left corner in each panel. The derived Spearman's rank order correlation coefficients and their statistical significance are +0.726, 2.0×10^{-6} (top), +0.601, 2.1×10^{-4} (middle) and +0.329, 1.6×10^{-1} (bottom).
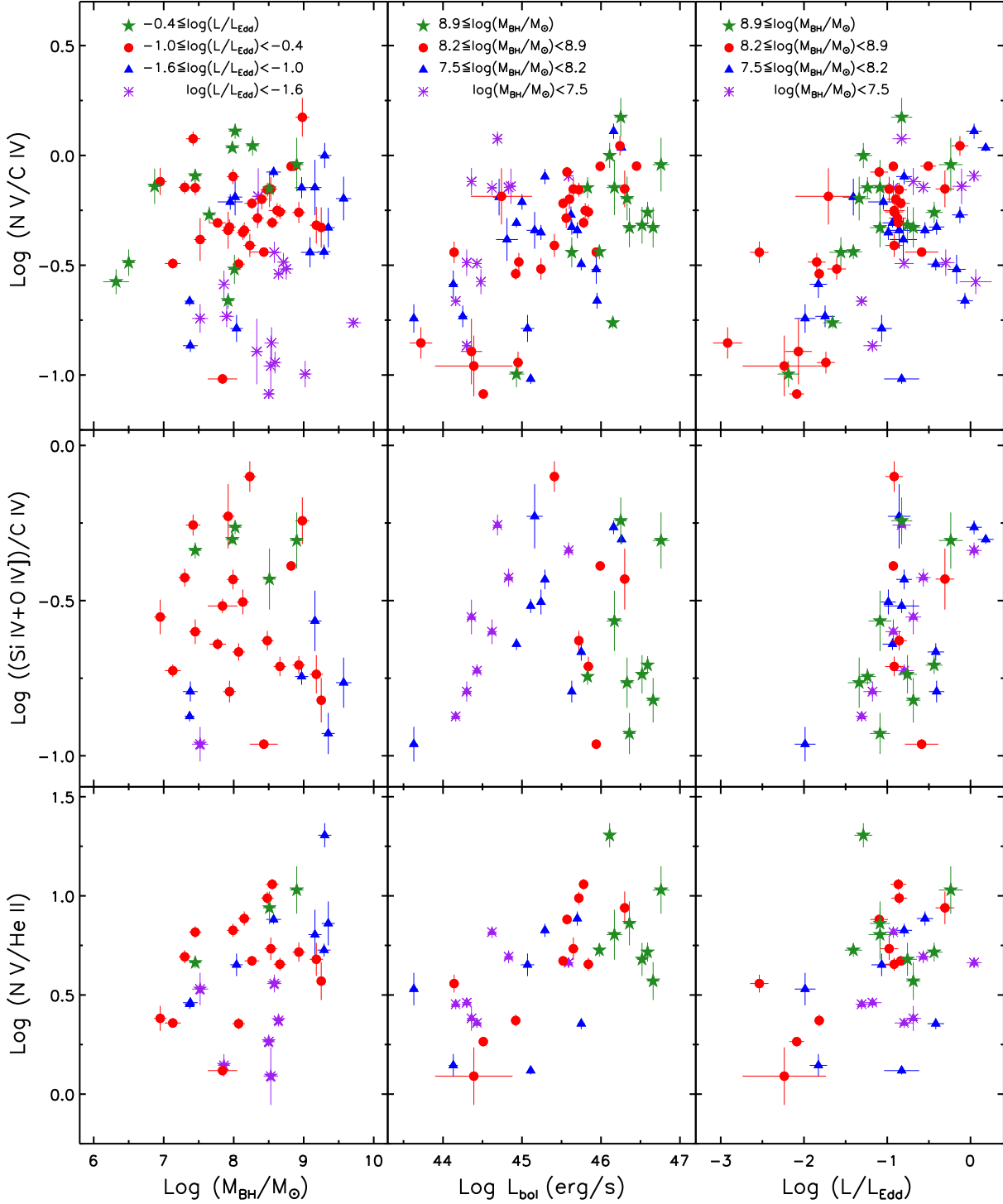
FIG. 7.— The relation between metallicity indicators and AGN properties (M_{BH}, L_{bol}, and L_{bol}/L_{Edd}). The symbols and colors represent the Eddington ratio or mass bin as indicated in the top panels.

shift evolution and the origin of the metallicity scaling relations in AGNs. In Figure 8, we overplot the metallicity indicators as functions of M_{BH} and L/L_{Edd} for high-z QSOs adopted from (Matsuoka et al. 2011b), along with the measurements of low-z QSOs. The low-z objects are more dispersed than high-z objects, partly because of the larger measurement uncertainties of the low-z objects. Note that the emission line fluxes were measured for individual objects in the low-z sam-

ple, while the composite spectra of high-z QSOs in each black hole mass and Eddington ratio bin were used for the emission line flux measurements (see Matsuoka et al. 2011b).

Interestingly, the low-z and high-z samples appear to show different trends in Figure 8 (top panels). As mentioned in §4.3, the low-z sample shows only marginal correlations between metallicity indicators and M_{BH}, while the high-z sample clearly shows positive correlations of metallicity indica-

Flux ratio (1)	$M_{\rm BH}$ (2)	$L_{\rm bol}$ (3)	$L_{\rm bol}/L_{\rm Edd}$ (4)
N V/C IV	$r_{\rm S} = +0.076$	$r_{\rm S} = +0.487$	$r_{\rm S} = +0.473$
	$p = 5.3 \times 10^{-1}$	$p = 2.1 \times 10^{-5}$	$p = 3.6 \times 10^{-5}$
(Si IV+O IV])/C IV	$r_{\rm S} = -0.128$	$r_{\rm S} = +0.038$	$r_{\rm S} = +0.381$
	$p = 4.8 \times 10^{-1}$	$p = 8.4 \times 10^{-1}$	$p = 2.9 \times 10^{-2}$
N V/He II	$r_{\rm S} = +0.417$	$r_{\rm S} = +0.622$	$r_{\rm S} = +0.311$
	$p = 1.6 \times 10^{-2}$	$p = 1.1 \times 10^{-4}$	$p = 7.8 \times 10^{-2}$
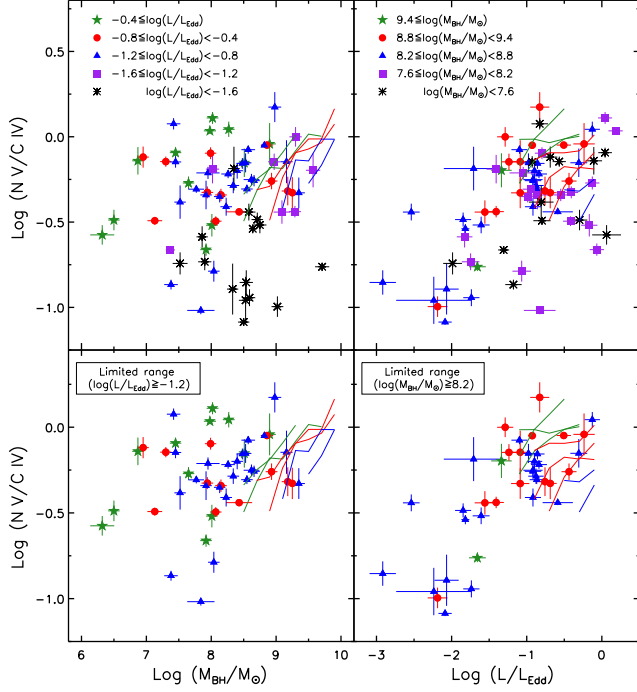
FIG. 8.— *Top:* Metallicity indicator (N V/C IV flux ratio) as functions of $M_{\rm BH}$ (left) and $L/L_{\rm Edd}$ (right). Low-z QSOs are represented with various symbols while high-z QSOs are denoted by solid lines (Matsuoka et al. 2011b). The colors represent different mass and Eddington ratios as indicated in the upper panels. *Bottom:* Metallicity indicator vs. $M_{\rm BH}$ (left) and $L/L_{\rm Edd}$ (right), after excluding low $M_{\rm BH}$ and low Eddington AGNs from low-z sample for proper comparison.

tors with $M_{\rm BH}$. On the other hand, the metallicity indicators of the low-z sample show much stronger positive correlations with $L/L_{\rm Edd}$ than with $M_{\rm BH}$, while the correlations between metallicity indicators and $L/L_{\rm Edd}$ are less evident in the high-z sample.

The difference in the trend with Eddington ratios between low-z and high-z samples is partly caused by the much wider range of $L/L_{\rm Edd}$ ($-3 < \log[L/L_{\rm Edd}] < 0$) covered by the low-$z$ sample than that covered by the high-z sample ($-1 < \log[L/L_{\rm Edd}] < 0$). As shown in Figure 8, low-z AGNs with $\log[L/L_{\rm Edd}] < -1.5$ (that is not covered in the high-z sample) show systematically lower N V/C IV flux ratios, leading to the more evident dependence on $L/L_{\rm Edd}$. Therefore, our results do not necessarily suggest that the $L/L_{\rm Edd}$ dependence on the metallicity indicators is systematically different between low-z and high-z QSOs. For proper comparison, low Eddington AGNs ($\log[L/L_{\rm Edd}] < -1.5$) are required at high-$z$. These results imply that the accretion activity of black holes are closely related with metal enrichment at the central part of host galaxies.

The dependence of metallicity indicators on $M_{\rm BH}$ appears to be different between the low-z and high-z samples. At high-z, more massive AGNs have higher metallicity although the $M_{\rm BH}$ range is small ($8.5 < \log M_{\rm BH} < 10$). In contrast, the low-$z$ sample shows much larger scatter without clear trend between $M_{\rm BH}$ and metallicity indicators. However, the large scatter in the low-z sample is partly caused by the low Eddington AGNs, which have systematically lower N V/C IV flux ratios, as described as the metallicity-Eddington ratio relation. However, if AGNs with similar Eddington ratios are selected (e.g., same color objects in Figure 8), then there appears to be a weak trend of metallicity with $M_{\rm BH}$, suggesting that at low-z, $Z_{\rm BLR}$ has weak dependency on $M_{\rm BH}$ at fixed Eddington ratios.

For high-z QSOs, the tightness of the observed $Z_{\rm BLR} - M_{\rm BH}$ correlation is probably caused by the limited range of the Eddington ratios since only high Eddington QSOs were included in the high-z sample. However, inclusion of low Eddington AGNs will presumably weaken the correlation as in the case of the low-z sample. As a consistency check, we match the ranges of $M_{\rm BH}$ and Eddington ratio between high-z and low-z samples, by excluding low $M_{\rm BH}$ and low Eddington objects from the low-z sample as presented in the bottom panels of Figure 8. As expected, both high-z and low-z samples in the matched dynamical range show similar metallicity dependency on both $M_{\rm BH}$ and Eddington ratio although the $M_{\rm BH}$-$Z_{\rm BLR}$ relation is much weaker in low-z than at in high-z.

Our results imply that the BLR metallicity of low-z AGNs mainly depends on the Eddington ratio, and weakly depends on $M_{\rm BH}$. Currently, it is unknown how $Z_{\rm BLR}$ scales with average gas metallicity of host galaxies. Nevertheless, the observed metallicity dependency on $M_{\rm BH}$ may imply that there is connection among BH growth, gas enrichment, and galaxy evolution.

Assuming that $Z_{\rm BLR}$ correlates with gas metallicity of host galaxies, we try to understand the observed relations with several scenarios. The correlation between $M_{\rm BH}$ and $Z_{\rm BLR}$ at high-z can be interpreted as a consequence of the combination of the galaxy mass-metallicity relation and the $M_{\rm BH} - M_{\rm bulge}$ relation (Warner et al. 2003; Matsuoka et al. 2011b). For QSOs at $z \sim 2 - 3$ that corresponds to the peak of the quasar activity in the cosmological timescale, it has been often claimed that the major merger triggers the AGN activity through the efficient mass fueling onto black holes (Hasinger 2008; Li et al. 2010). Here the major merger event reduces the angular momentum of gas clouds at the nuclear regions of the quasar host galaxies, providing efficient mass fueling. In this case, the metallicity of accreting gas onto the nucleus may be characterized by the mass-metallicity relation of the host galaxy. Regarding the black hole to host galaxy connection, the $M_{\rm BH} - M_{\rm bulge}$ relation has not been observationally defined at high-z although several studies indicated that $M_{\rm BH}$-to-$M_{\rm bulge}$ ratio increases with redshift (e.g., Woo et al. 2006, 2008; Bennert et al. 2010, 2011; Merloni et al. 2010). Thus, if we assume a scaling relation between $M_{\rm BH}$ and galaxy mass, presumably with higher normalization than the local $M_{\rm BH}$-$M_{\rm bulge}$ relation, then black hole mass scales with both stellar mass and gas metallicity, hence the $M_{\rm BH}$-$Z_{\rm BLR}$ relation is naturally expected at high-z.

The weaker correlation of $M_{\rm BH}$ with $Z_{\rm BLR}$ at low-z can be interpreted as combination of two additional effects. First, gas metallicity increased from high-z to low-z by further star formation after major BH growth. In other words, for the same galaxy mass (or black hole mass), metallicity has been in-

creased, particularly at the nuclear region, leading to higher metallicity at fixed M_{BH} compared to high-z objects. For example, nuclear star formation induced by secular process (e.g., bar instability) and galaxy interaction may sufficiently increase metallicity (e.q., Maiolino et al. 2008). Another difference between low-z and high-z is the gas fraction, especially for massive galaxies like quasar host galaxies. The minor merger process is more important as an AGN triggering mechanism at low-z (e.q., Taniguchi 1999; Cisternas et al. 2011). Thus, as a consequence of minor mergers between a gas-poor massive galaxy (i.e., a quasar host galaxy) and a relatively gas-rich less-massive galaxy, the metallicity of accreting gas onto the nucleus can be largely affected by the chemical property of the merging, less-massive galaxy. In this case, the metallicity of accreting gas does not simply reflect the mass-metallicity relation of the host galaxy. Second, the M_{BH}-to-M_{bulge} ratio may change over cosmic time. If black hole mass was higher at fixed stellar mass at high-z, then by combining galaxy mass-metallicity relation and $M_{BH} - M_{bulge}$ relation, we may expect similar M_{BH}-metallicity relation in low-z, but with a different normalization. In other words, at fixed metallicity, M_{BH} is lower in low-z than in high-z. Although it is beyond the scope of the current work to quantify and compare these two effects, it is reasonable to conclude that coupling between black hole mass with gas metallicity becomes much weaker with decreasing redshift.

6. SUMMARY & CONCLUSION

To investigate the chemical properties of low-z QSOs, we measured the flux ratios of the rest-frame UV emission lines as metallicity indicators using a sample of 70 low-z PG QSOs at $z < 0.5$. By comparing BLR gas metallicity with black hole mass, luminosity and Eddington ratio, we find that Z_{BLR} correlates with Eddington ratio while Z_{BLR} shows much weaker correlation with M_{BH}, indicating that the metal enrichment at the central part of host galaxies is closely connected to the accretion activity of AGN. These trends are different from high-z QSOs, which shows a tighter correlation between Z_{BLR} and M_{BH} and a weaker correlation between Z_{BLR} and Eddington ratio. The apparent difference between low-z and high-z samples seems to be caused by the limited dynamical range in the high-z sample. Various star formation mechanism can increase BLR gas metallicity the cosmic time, increasing the scatter in the metallicity correlation with properties of AGN in low-z.

REFERENCES

Araki, N., Nagao, T., Matsuoka, K., et al. 2012, A&A, 543, A143
Baldwin, J. A., & Netzer, H. 1978, ApJ, 226, 1
Baskin, A., & Laor, A. 2005, MNRAS, 356, 1029
Bennert, V. N., Auger, M. W., Treu, T., Woo, J.-H., & Malkan, M. A. 2011, ApJ, 742, 107
Bennert, V. N., Treu, T., Woo, J.-H., et al. 2010, ApJ, 708, 1507
Boroson, T. A. 2002, ApJ, 565, 78
Boyle, B. J. 1990, MNRAS, 243, 231
Cisternas, M., Jahnke, K., Inskip, K. J., et al. 2011, ApJ, 726, 57
Corbin, M. R. 1997, ApJS, 113, 245
Danforth, C. W., Keeney, B. A., Stocke, J. T., Shull, J. M., & Yao, Y. 2010, ApJ, 720, 976
Denney, K. D., Peterson, B. M., Pogge, R. W., et al. 2010, ApJ, 721, 715
Dietrich, M., Hamann, F., Shields, J. C., et al. 2003, ApJ, 589, 722
Dietrich, M., Mathur, S., Grupe, D., & Komossa, S. 2009, ApJ, 696, 1998
Dietrich, M., & Wilhelm-Erkens, U. 2000, A&A, 354, 17
Dietrich, M., Appenzeller, I., Wagner, S. J., et al. 1999, A&A, 352, L1
Erb, D. K., Shapley, A. E., Pettini, M., et al. 2006, ApJ, 644, 813
Ferland, G. J., Baldwin, J. A., Korista, K. T., et al. 1996, ApJ, 461, 683
Gallazzi, A., Charlot, S., Brinchmann, J., White, S. D. M., & Tremonti, C. A. 2005, MNRAS, 362, 41
Groves, B. A., Heckman, T. M., & Kauffmann, G. 2006, MNRAS, 371, 1559
Grupe, D. 2004, AJ, 127, 1799
Hamann, F., & Ferland, G. 1992, ApJ, 391, L53
—. 1993, ApJ, 418, 11
Hamann, F., Korista, K. T., Ferland, G. J., Warner, C., & Baldwin, J. 2002, ApJ, 564, 592
Hasinger, G. 2008, A&A, 490, 905
Juarez, Y., Maiolino, R., Mujica, R., et al. 2009, A&A, 494, L25
Korista, K., Baldwin, J., & Ferland, G. 1998, ApJ, 507, 24
Kurk, J. D., Walter, F., Fan, X., et al. 2007, ApJ, 669, 32
Laor, A., Bahcall, J. N., Jannuzi, B. T., et al. 1994, ApJ, 420, 110
Laskar, T., Berger, E., & Chary, R.-R. 2011, ApJ, 739, 1
Li, Y.-R., Wang, J.-M., Yuan, Y.-F., Hu, C., & Zhang, S. 2010, ApJ, 710, 878
Maiolino, R., Nagao, T., Grazian, A., et al. 2008, A&A, 488, 463
Mannucci, F., Cresci, G., Maiolino, R., Marconi, A., & Gnerucci, A. 2010, MNRAS, 408, 2115
Mannucci, F., Cresci, G., Maiolino, R., et al. 2009, MNRAS, 398, 1915
Matsuoka, K., Nagao, T., Maiolino, R., Marconi, A., & Taniguchi, Y. 2009, A&A, 503, 721
—. 2011a, A&A, 532, L10
Matsuoka, K., Nagao, T., Marconi, A., Maiolino, R., & Taniguchi, Y. 2011b, A&A, 527, A100

Merloni, A., Bongiorno, A., Bolzonella, M., et al. 2010, ApJ, 708, 137
Mortlock, D. J., Warren, S. J., Venemans, B. P., et al. 2011, Nature, 474, 616
Nagao, T., Maiolino, R., De Breuck, C., et al. 2012, A&A, 542, L34
Nagao, T., Maiolino, R., & Marconi, A. 2006a, A&A, 447, 863
Nagao, T., Marconi, A., & Maiolino, R. 2006b, A&A, 447, 157
Nagao, T., Murayama, T., Shioya, Y., & Taniguchi, Y. 2002, ApJ, 575, 721
Onken, C. A., Ferrarese, L., Merritt, D., et al. 2004, ApJ, 615, 645
Osmer, P. S. 1980, ApJS, 42, 523
Panter, B., Jimenez, R., Heavens, A. F., & Charlot, S. 2008, MNRAS, 391, 1117
Park, D., Kelly, B. C., Woo, J.-H., & Treu, T. 2012, ApJS, 203, 6
Peterson, B. M., Ferrarese, L., Gilbert, K. M., et al. 2004, ApJ, 613, 682
Savaglio, S., Glazebrook, K., Le Borgne, D., et al. 2005, ApJ, 635, 260
Schmidt, M., & Green, R. F. 1983, ApJ, 269, 352
Shemmer, O., & Netzer, H. 2002, ApJ, 567, L19
Shemmer, O., Netzer, H., Maiolino, R., et al. 2004, ApJ, 614, 547
Shen, Y., Greene, J. E., Strauss, M. A., Richards, G. T., & Schneider, D. P. 2008, ApJ, 680, 169
Shields, G. A. 1976, ApJ, 204, 330
Storchi-Bergmann, T., Schmitt, H. R., Calzetti, D., & Kinney, A. L. 1998, AJ, 115, 909
Taniguchi, Y. 1999, ApJ, 524, 65
Tremonti, C. A., Heckman, T. M., Kauffmann, G., et al. 2004, ApJ, 613, 898
Uomoto, A. 1984, ApJ, 284, 497
Vanden Berk, D. E., Richards, G. T., Bauer, A., et al. 2001, AJ, 122, 549
Vestergaard, M., & Peterson, B. M. 2006, ApJ, 641, 689
Warner, C., Hamann, F., & Dietrich, M. 2003, ApJ, 596, 72
—. 2004, ApJ, 608, 136
Warner, C., Hamann, F., Shields, J. C., et al. 2002, ApJ, 567, 68
Wilkes, B. J. 1984, MNRAS, 207, 73
Wills, B. J., Brotherton, M., Laor, A., et al. 1999, in Astronomical Society of the Pacific Conference Series, Vol. 162, Quasars and Cosmology, ed. G. Ferland & J. Baldwin, 373
Woo, J.-H., Treu, T., Malkan, M. A., & Blandford, R. D. 2006, ApJ, 645, 900
—. 2008, ApJ, 681, 925
Woo, J.-H., & Urry, C. M. 2002, ApJ, 579, 530
Woo, J.-H., Treu, T., Barth, A. J., et al. 2010, ApJ, 716, 269
Yabe, K., Ohta, K., Iwamuro, F., et al. 2012, PASJ, 64, 60